chemosensors

MDPI

*Article*

# Nickel-Doped ZnO Porous Sea Urchin Nanostructures with Various Amounts of Oxygen Defects for Volatile Organic Compound Detection

**Haibo Ren [1,*], Huaipeng Weng [1], Xumeng Dong [1], Jiarui Huang [2,*] and Sang Woo Joo [3,*]**

[1] School of Materials Science and Engineering, Anhui Polytechnic University, Wuhu 241000, China
[2] Key Laboratory of Functional Molecular Solids of the Ministry of Education, Anhui Laboratory of Molecule-Based Materials, College of Chemistry and Materials Science, Anhui Normal University, Wuhu 241002, China
[3] School of Mechanical Engineering, Yeungnam University, Gyeongsan 712749, Gyeoungbuk, Republic of Korea
* Correspondence: renhaibo@ahpu.edu.cn (H.R.); jrhuang@mail.ahnu.edu.cn (J.H.); swjoo@yu.ac.kr (S.W.J.)

**Abstract:** Porous sea urchin-like nickel-doped ZnO with various nickel contents and high specific surface area were synthesized using a solution method followed by calcination. The nickel-doped ZnO products consisted of numerous porous nanoleaves. The Ni content in these products ranged from 5% to 20%. The Ni dopants in the ZnO lattice were verified by X-ray diffraction and X-ray photoelectron spectroscopy. The sensors based on nickel-doped ZnO sea urchins showed superior sensing performance for some volatile organic compounds (VOCs). ZnO sea urchins with 10% nickel doping exhibited the best gas-sensing performance, including a low working temperature, short response/recovery time, and high sensor response. In particular, the 10% Ni-doped ZnO sea urchin sensor exhibited a response of 84.4 with response/recovery times of 17/20 s towards 100 ppm formaldehyde vapor. These superior sensing behaviors were attributed mainly to a suitable Ni content with high content of oxygen defects, small nanocrystals, and a porous hierarchical structure with a high specific surface area.

**Keywords:** zinc oxide; nickel doping; zinc hydroxide carbonate; nanoleaf; gas sensor; volatile organic compounds



**Citation:** Ren, H.; Weng, H.; Dong, X.; Huang, J.; Joo, S.W. Nickel-Doped ZnO Porous Sea Urchin Nanostructures with Various Amounts of Oxygen Defects for Volatile Organic Compound Detection. *Chemosensors* **2023**, *11*, 223. https://doi.org/10.3390/chemosensors11040223

Academic Editor: Boris Lakard

Received: 11 February 2023
Revised: 25 March 2023
Accepted: 2 April 2023
Published: 4 April 2023



## 1. Introduction

Volatile organic compounds (VOCs) are often emitted from decoration and building materials. As the gaseous toxins are widespread in both indoors and outdoors settings, prolonged exposure to VOCs causes harm to the eyes and damages the nervous system, causing a series of diseases [1]. Moreover, VOCs at low concentrations can easily cause serious respiratory problems. For example, formaldehyde at very low concentrations (0.75 ppm) can cause cancer [2]. Therefore, convenient gas sensors with a low detection limit, high response, and low energy consumption are needed urgently. A variety of metal oxide semiconductors that function as excellent sensing materials, such as $SnO_2$ [3], ZnO [4], $In_2O_3$ [5], $Fe_2O_3$ [6], NiO [7], and $V_2O_5$ [8], were developed for detecting volatile harmful gases. Among the metal oxide semiconductors, ZnO, a typical n-type semiconductor, possesses a direct bandgap of 3.37 eV. ZnO has drawn considerable attention due to its physical/chemical stability, easy preparation, abundance, high electron mobility, and excellent electric conductivity [9,10]. It is currently being used for detecting various flammable, volatile, and harmful gases [11–14]. On the other hand, for a pure ZnO sensing material, the high detection limit, high working temperature, and low response greatly limit the widespread applications of ZnO sensors. Therefore, it is urgent to develop new ZnO-based sensors with relatively low working temperature, high sensitivity, and good selectivity.

Some strategies were adopted to overcome the above problems. The morphology of ZnO partially affects the sensitivity, working temperature, and response rate of gas sensing

behaviors. Especially, a 3D porous structure with a high surface area could provide numerous surface active sites for accepting more gas molecules and holding surface chemical reactions. Another strategy for improving gas-sensing behaviors is associated with the surface decoration of noble metals and doping ZnO with different metal elements. The commonly adopted noble metals Pt [15], Pd [16], Ag [17], and Au [18] are adopted for modification of the ZnO surface. They can greatly optimize the sensing behaviors of the gas sensor by improving the catalytic activity of the sensing materials. Despite the obvious improvement in the sensitivity to VOCs, the high cost of noble metals has limited their wider applications as gas-sensing materials. Therefore, doping with different elements (e.g., Fe [19], Co [20], Ni [21], Cu [22], and Al [23]) of low cost and wide availability is considered as one of the practical strategies to enhance the sensing performance of ZnO. For example, Mo et al. prepared a mesoporous Co-doped ZnO hierarchical structure by the calcination of its precursor [20]. The 5% Co-doped ZnO hierarchical structure sensor exhibited a sensitivity of 54 towards 50 ppm ethanol at 180 °C. El Khalidi et al. synthesized various Ni-doped ZnO films by spray pyrolysis [21]. Among them, the 2% Ni-doped ZnO film sensor showed the best gas-sensing performance, with the highest sensitivity (90) for 100 ppm acetone at 450 °C. The response and recovery times were 50 s and 90 s, respectively. Of the various metal dopants, Ni-doped ZnO has exceptional features. Ni could induce a spillover–sensitization effect [21]. $Ni^{2+}$-doped ZnO produces more donor defects and can increase the level of adsorbed gas molecules. In addition, it can facilitate the ionization of gas molecules and the dissociation of targeted gases from the surface of the sensing materials, leading to higher sensitivity and rapid response/recovery behaviors in ZnO sensors. The empty 3d orbital in $Ni^{2+}$ allows the production of more oxygen vacancies when $Zn^{2+}$ is replaced with $Ni^{2+}$. Thus, the transportation of charges accelerates and the number of adsorbed oxygen anions increases significantly [24].

So far, some strategies have been adopted for preparing the doped ZnO with various nanostructures, including co-precipitation [24], spray pyrolysis [25], the hydrothermal method [26], the sol–gel method [27], high-temperature calcination [28], RF sputtering [29], and the electrospinning method [30]. Kamble et al. fabricated various Ni-doped content nanorod-like ZnO nanostructure sensors by a co-precipitation method [24]. The 2% Ni-ZnO nanorod sensor presented a response of 356 at 200 °C. The detected gas was $NO_2$ gas with 100 ppm. Modaberi et al. prepared a Ni-doped content nanorod-like ZnO nanostructure by calcining the precursor [28]. The 8% Ni-doped nanorod-like ZnO sensor exhibited the highest response towards $H_2S$ (100 ppm) gas at 200 °C. The response value reached 45.3. Among the synthetic methods of Ni-doped ZnO, the cooperation of an aqueous solution method and calcination treatment has attracted much attention because of its simple operation, low cost, and easy synthesis. Thus far, a high content of Ni-doped porous sea urchin-like ZnO nanostructures assembled from numerous nanosheets has rarely been achieved using an aqueous solution method and a subsequent heat treatment. The effect of ZnO doped with a high concentration of Ni on the sensitivity of gas sensors also needs to be investigated.

In this study, porous sea urchin-like ZnO nanostructures with various Ni doping contents were prepared using an aqueous solution method and a subsequent heat treatment. The sensing performance of the Ni-doped ZnO sea urchins towards VOCs was also studied. Compared to other VOCs, the Ni-doped ZnO sea urchin sensors exhibited a strong response to formaldehyde vapor. The Ni doping and unique porous sea urchin-like structure promote an outstanding sensing property. The mechanism of the gas-sensing behavior to formaldehyde vapor is also discussed.

## 2. Experimental Details

### *2.1. Synthesis of Ni-Doped ZnO Nanostructures*

Porous Ni-doped ZnO nanostructures were synthesized as follows. Briefly, 0.0211 g of $NiCl_2 \cdot 6H_2O$ and 0.5021 g of $Zn(NO_3)_2 \cdot 6H_2O$ were dissolved in 35 mL of deionized water; the atomic ratio of Ni and Zn was 0.5:9.5. A saturated $NH_4HCO_3$ solution was

then prepared. The pH was adjusted to 6.5 by introducing $CO_2$ gas for approximately 3 h. Subsequently, 15 mL of the saturated $NH_4HCO_3$ solution was poured into the previously prepared 35 mL solution under stirring, and then was placed at a temperature atmosphere of 6 °C for 8 h. After that, the precursor was collected after washing and dried at 50 °C for 15 h. The 5% Ni-doped ZnO nanostructure was obtained by high-temperature calcination at 350 °C for 1 h. The 10% Ni-doped ZnO sample, the 15% Ni-doped ZnO sample, and the 20% Ni-doped ZnO sample were synthesized using a similar procedure to that of the 5% Ni-doped ZnO sample, with the amount of $NiCl_2 \cdot 6H_2O$ changed from 0.0211 g to 0.0446 g, 0.0708 g, and 0.0997 g, respectively. The synthesis of the pure ZnO sample was similar to that of the 5% Ni-doped ZnO sample without adding $NiCl_2 \cdot 6H_2O$.

### *2.2. Material Characterization*

The products were characterized by X-ray diffraction (XRD, Shimadzu XRD-6000, Shimadzu, Kyoto, Japan) using high-intensity Cu Kα radiation with a wavelength of 1.54178 Å, field-emission scanning electron microscopy (FESEM, Hitachi S-4800, Hitachi, Kyoto, Japan, operated at 5 kV), high-resolution transmission electron microscopy (HRTEM, JEOL-2010 TEM, JEOL, Kyoto, Japan) with an acceleration voltage of 200 kV, thermogravimetric analysis (TGA, NETZSCH STA449C, NETZSCH, Selb, Germany), and $N_2$ adsorption–desorption isotherm measurements (Nova 2000E, Quantachrome, Boynton Beach, FL, USA). The pore size distribution was determined from the desorption branch of the isotherm using the Barrett–Joyner–Halenda (BJH) method. The TGA was carried out in air with a set heating rate (10 °C $min^{-1}$) in the temperature scope (room temperature to 600 °C). X-ray photoelectron spectroscopy (XPS, ESCALAB 250, ESCALAB, Ciudad de México, México) was also performed. The elemental distribution of the products was determined by energy dispersive spectroscopy (FESEM, Hitachi S-4800, operated at 15 kV).

### *2.3. Fabrication and Testing of the Gas Sensor*

Figure S1 in the Supplementary Material presents the experimental device for gas-sensing measurements. The fabrication process of the gas sensors was as follows: 0.1 g of porous sea urchin-like 5% Ni-ZnO, 10% Ni-ZnO, 15% Ni-ZnO, and 20% Ni-ZnO composites, and porous sea urchin-like ZnO were dispersed in a 0.5 mL ethanol solution to obtain a uniform suspension. The above suspension was smeared uniformly on the outer surface of the tube-shaped substrate made from aluminum, where a pair of Au electrodes was tightly printed on the bottom of the aluminum-made substrate. The as-prepared sensors were dried in air at 60 °C for 3 h, followed by high-temperature calcination of 280 °C for 2 h. Subsequently, the working temperature for the gas sensors can be achieved by placing a Ni-Cr heating coil into the ceramic tube, as shown in Figure S2a. The sensor was kept at 280 °C for two days in air to improve its long-term stability. A stationary-state gas distribution method was used to test the gas response. The sensor response measurement was performed on an electrochemical workstation (CHI-660E, Shanghai Chenhua Instruments Co., Ltd., Shanghai, China) using chronoamperometry at 0.7 V. Figure S2b presents a diagram of the testing principle of the gas-sensing measurement system. Detecting gases, such as ethanol vapor (headspace vapor of ethanol), formaldehyde vapor (headspace vapor of a 38.5 wt.% formaldehyde solution), and $NH_3/N_2$ mixtures (1 vol%), were injected into a test chamber (1000 mL) and mixed with air. To detect 1 ppm of ethanol vapor, formaldehyde vapor, and $NH_3$, 0.017 mL headspace vapor of ethanol, 1.0 mL headspace vapor of a 38.5 wt.% formaldehyde solution, and 0.1 mL $NH_3/N_2$ mixtures were injected into the test chamber, respectively. The response of the sensor was defined as $R_a/R_g$ (reducing gases), where $R_a$ is the resistance of the sensor in dry air and in dry air mixed with the test gases. In the measurement system, the response was also calculated using the following equation: $I_a/I_g$, where $I_g$ and $I_a$ are the output currents in the test gas and air, respectively. The response or recovery time is expressed as the time required for the sensor output to reach 90% saturation after applying or switching off the gas in a step function.

## 3. Results and Discussion

### *3.1. Structural and Morphological Characterization*

Figures 1a and S3a show the characteristic diffraction peaks of the precursors. All XRD peaks of the samples corresponded to the crystal planes of the monoclinic $Zn_5(CO_3)_2(OH)_6$ (JCPDS no. 19-1458). After heat treatment in air, the XRD patterns of all Ni-doped ZnO products displayed in Figures 1a and S3a could be assigned to hexagonal ZnO (JCPDS no. 36-1451). The XRD pattern of the 20% Ni-doped ZnO sample showed a very weak peak at approximately 43.3°, which was ascribed to the crystal plane (200) of bunsenite NiO (JCPDS no. 47-1049). No other obvious peaks related to nickel compounds were observed in the XRD patterns of the ZnO products doped with different nickel contents, indicating that nickel ions systematically enter the lattice without destroying the original crystal structure of ZnO. The mean crystallite size of ZnO crystallites could be calculated using the Scherer formula:

$$D = \frac{0.9\lambda}{\beta \cdot \cos\theta} \quad (1)$$

where $\lambda$, $\beta$, and $\theta$ are the wavelength of the X-ray beam, width at half maximum, and diffraction angle, respectively. The mean crystallite size of the 0%, 5%, 10%, 15%, and 20% Ni-ZnO sea urchins were 18.2 nm, 15.1 nm, 12.5 nm, 15.3 nm, and 14.0 nm, respectively. The lattice constants of the samples listed in Table S1 are comparable with standard data. a (a = b) and c were extracted from the peaks (002) and (100). The calculated lattice parameters decreased with the increase of Ni content, which refers to the substitution of $Zn^{2+}$ with $Ni^{2+}$ with the ionic radius of nickel (0.055 nm) slightly smaller than that of zinc (0.060 nm). However, the calculated lattice parameters increased after 10% Ni, which may be due to the formation of a NiO phase decreasing the amount of Ni dopants.

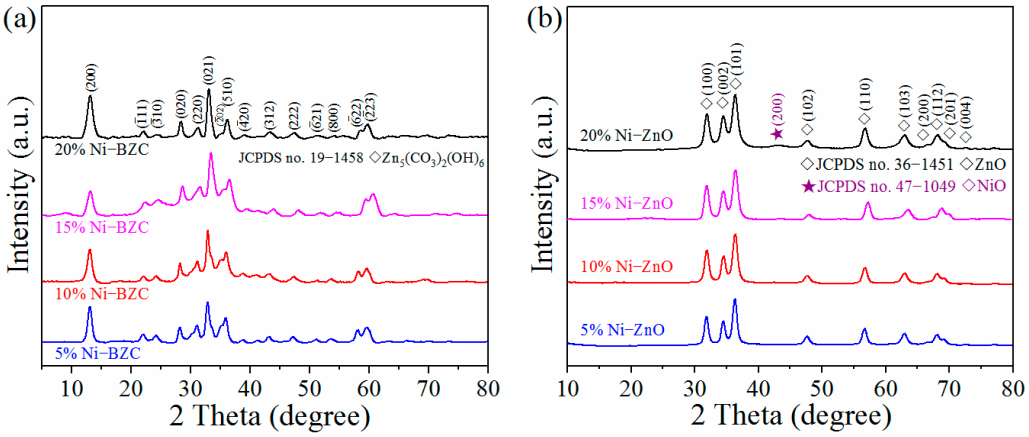


**Figure 1.** XRD patterns of (**a**) Ni-doped $Zn_5(CO_3)_2(OH)_6$ precursors and (**b**) Ni-doped ZnO products.

Furthermore, Figure S3b shows the EDS analysis of the 10% Ni-ZnO product. Only Zn, Ni, and O were observed, suggesting that the final product was Ni-doped ZnO.

Figures 2 and S4 present SEM images of the sea urchin-like Ni-doped $Zn_5(CO_3)_2(OH)_6$ precursor before and after calcination. Observing the SEM images shown in Figure 2a,b, the precursors exhibited a sea urchin-like structure with a mean diameter of 4–5 μm. The unique structure comprised numerous nanoleaves with a mean thickness of ~12 nm. These nanoleaves with smooth surfaces grew perpendicularly outward to form the sea urchin-like structure. After calcination in air, the 10% Ni-ZnO sample maintained the sea urchin-like morphology, as shown in Figure 2c,d. With increasing Ni content in the Ni-ZnO sea urchins, the mean diameter of the sea urchin-like Ni-ZnO becomes larger. In Figure S4a,c,e, we can find that 5%, 15%, and 20% Ni-doped $Zn_5(CO_3)_2(OH)_6$ precursors all showed similar structures: a sea urchin-like morphology. Numerous ultrathin nanoleaves lead to the unique structure in a self-assembling manner. The sea urchin-like morphology was retained after the calcination of the products, as shown in Figure S4b,d,f. The EDS mapping

images of 10% Ni-ZnO sea urchins are exhibited in Figure S5. Ni, Zn, and O were dispersed uniformly in nano-sea urchins. The morphologies of the precursors (basic zinc carbonate) and the pure ZnO products are exhibited in FESEM images (Figure S6). Obviously observed, the pure $Zn_5(CO_3)_2(OH)_6$ precursor also displays a sea urchin-like morphology, as shown in Figure S6a,b. This favorable structure is constructed by the self-assemble of abundant nanoleaves. The diameter of the pure ZnO precursors averages around 8.6 µm. FESEM images of the pure ZnO products are shown in Figure S6c,d. After calcination (450 °C, 2 h), the post-calcination sea urchin morphology is maintained without any damage to the morphology, which can be observed in the FESEM images (Figure S6c,d) of the pure ZnO products.

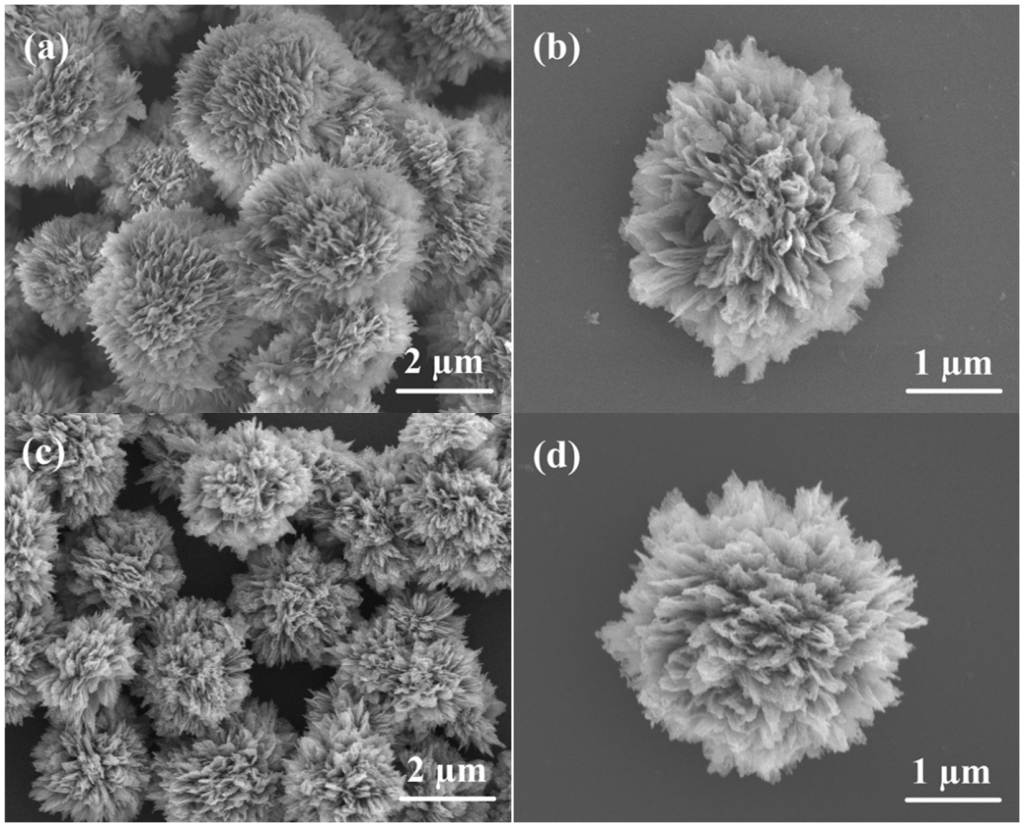


**Figure 2.** Representative SEM images of (**a**,**b**) the sea urchin-like 10% Ni-doped $Zn_5(CO_3)_2(OH)_6$ precursor and (**c**,**d**) the corresponding porous sea urchin-like Ni-doped ZnO.

The detailed structure of 10% Ni-doped ZnO sea urchins was studied further by transition electron microscopy (TEM). Figure 3a–c presents the TEM and HRTEM images of the sample. The sample had a sea urchin morphology composed of numerous ultra-small nanoleaves. There were many irregular nanopores on the nanoleaves (Figure 3b). These pores of various sizes were produced by the decomposition of the $Zn_5(CO_3)_2(OH)_6$ precursor to $CO_2$ gas and gaseous $H_2O$, which can improve the sensing performance. The interplanar distances were 0.281, 0.261, and 0.163 nm, which correspond to the hexagonal phase of ZnO planes (100), (002), and (110), respectively (Figure 3c) [31]. Figure 3d shows the selected area electron diffraction (SAED) pattern of the sample, which can be assigned to the (100), (101), (110), (103), (112), and (201) planes of hexagonal ZnO [32]. The TEM results were consistent with the structural and morphological characteristics of the 10% Ni-ZnO sample obtained from XRD (Figure 1b) and SEM (Figure 2).

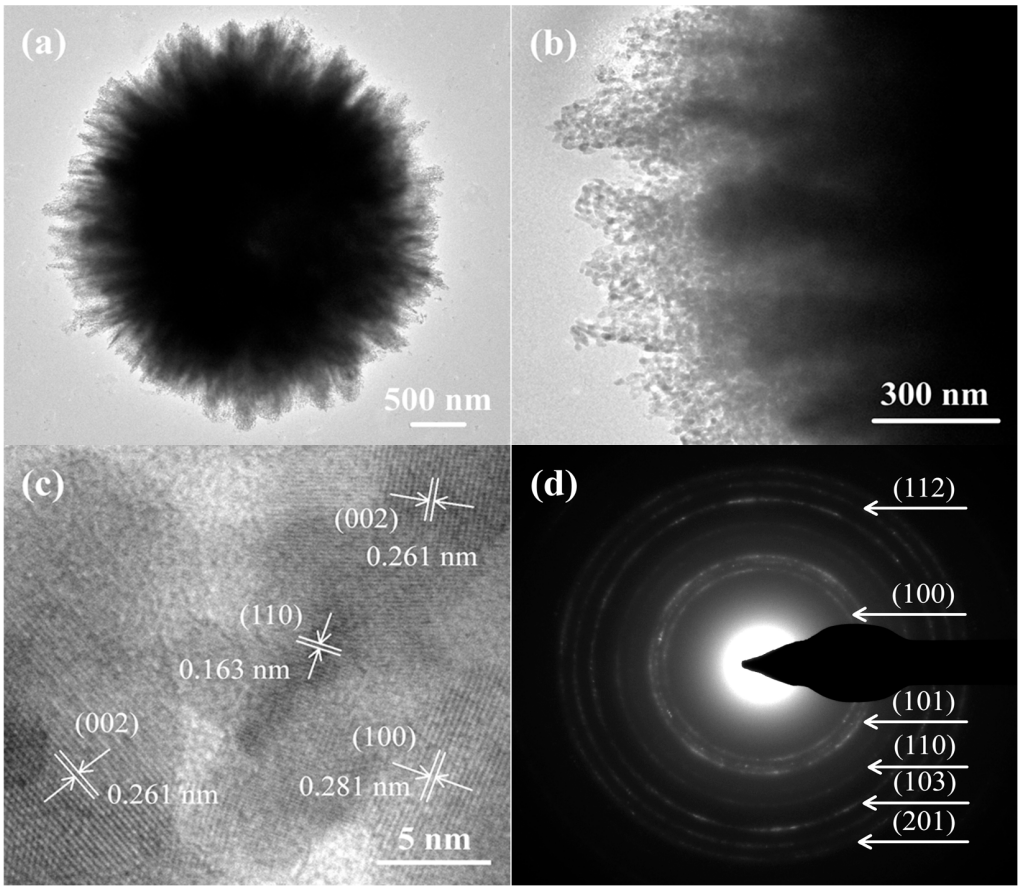


**Figure 3.** (**a**) TEM image, (**b**) high-magnification TEM image, (**c**) HRTEM image, and (**d**) SAED pattern of 10% Ni-doped ZnO sea urchins.

TGA was performed to study the thermal decomposition process of Ni-doped $Zn_5(CO_3)_2(OH)_6$ precursors (Figure S7). Before 180 °C, a slight mass loss occurred because of absorbed water. At temperatures from 180 °C to 400 °C, a mass loss of 27.9% occurred, which is consistent with the theoretical value of 28.8%. This is primarily because the Ni-doped $Zn_5(CO_3)_2(OH)_6$ precursors decomposed to Ni-doped ZnO, $CO_2$ gas, and gaseous $H_2O$. A large volume of $CO_2$ gas and gaseous $H_2O$ were released from the inner structure of the precursors, resulting in a large number of mesopores in the final products after calcination. These mesopores will significantly enhance the specific surface area of Ni-doped ZnO sea urchins and provide more available sites for catalytic redox reactions. The decomposition chemical equation can be described as follows:

$$Zn_5(CO_3)_2(OH)_6 = 5ZnO + 3H_2O \text{ (mass 13.8\%)} + 2CO_2 \text{ (mass 15.0\%)} \quad (2)$$

Figure S8 shows the FTIR spectra of 10% Ni-ZnO sea urchins and the corresponding precursor. The main characteristic peaks at 472, 837, 1416, and 1510 $cm^{-1}$ (Figure S8a) were attributed to the $CO_2^{3-}$ bending vibrations in the precursor. The peak at ca. 3391 $cm^{-1}$ can be assigned to the –OH group in the precursor. In the FTIR spectrum of 10% Ni-ZnO sea urchins (Figure S8b), a strong characteristic peak at 432 $cm^{-1}$ can be observed clearly because of the vibration of Ni–O and Zn–O in the Ni-doped ZnO [33,34]. Because some peaks referring to Ni–O in NiO overlapped with those of Zn–O in ZnO, there is only a characteristic peak ranging from 430 $cm^{-1}$ to 440 $cm^{-1}$ in the FTIR spectrum. The characteristic peaks associated with the $CO_2^{3-}$ bending vibrations have disappeared due to the thorough decomposition of carbonate in the precursor to $CO_2$ and $H_2O$. In addition, two weak peaks at 1386 and 1638 $cm^{-1}$ were associated with the O–H bending vibration of the $H_2O$ molecule absorbed on Ni-doped ZnO sea urchins [35,36]. The broadest peak was

found at approximately 3448 $cm^{-1}$. This peak is assigned to the stretching vibration of the O–H bond from the absorbed $H_2O$ molecule [33].

The $N_2$ adsorption–desorption isotherms of the samples are shown in Figures S9 and S10. A plot of the pore size distribution suggests that the overwhelming majority of pore sizes are distributed from around 1.2 to 29.7 nm. The specific surface areas of the 0%, 5%, 10%, 15%, and 20% Ni-ZnO sea urchins were 30.3 $m^2$ $g^{-1}$, 53.4 $m^2$ $g^{-1}$, 116.5 $m^2$ $g^{-1}$, 78.3 $m^2$ $g^{-1}$, and 15.8 $m^2$ $g^{-1}$, respectively. The 10% Ni-ZnO sea urchins exhibited the highest specific surface area, which is mainly due to their microstructure with different sizes and the effect of Ni dopants decreasing the crystal size of ZnO. As for 15% and 20% Ni-ZnO sea urchins, the NiO phase observed in the XRD patterns would reduce the amount of Ni dopant, resulting in a low specific surface area. The high specific surface area likely produces more metal vacancies and oxygen species on the surface and inside the porous structure, generating more unsaturated active sites [37].

Figure 4a shows the UV-Vis spectra of the porous Ni-ZnO and pure ZnO sea urchins. There is a distinct absorption peak at ca. 360 nm. In addition, the absorption intensity of Ni-doped ZnO sea urchins was higher than that of pure ZnO sea urchins within the wavelength range of 300–800 nm. Moreover, the Tauc equation of $\alpha h\upsilon = C(h\upsilon - E_g)^{1/2}$ was applied to estimate the bandgap of pure ZnO and Ni-ZnO sea urchins. As shown in Figure 4b, the calculated bandgap of the 5%, 10%, 15%, and 20% Ni-ZnO sea urchins were 2.91, 2.89, 2.92, and 2.93 eV, respectively, which are smaller than that of pure ZnO sea urchins (3.01 eV). This suggests that introducing the Ni dopant in ZnO leads to less energy for the electronic transition than the pure ZnO sea urchins. Compared with the pure ZnO sample, the decrease in the bandgap of Ni-doped ZnO samples is due to the formation of energy levels of the $^5D_4$ state of $Ni^{2+}$ under the $^3F_4$ state of $Zn^{2+}$, i.e., immediately decreasing the conduction band of the ZnO sample [24].

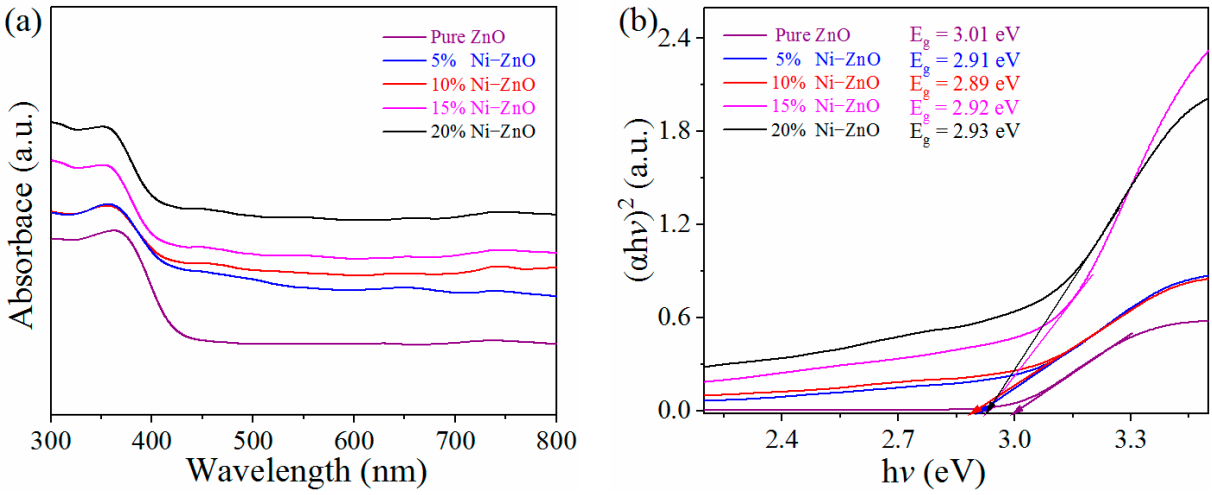


**Figure 4.** (**a**) UV-vis absorption spectra of the porous pure sea urchin-like ZnO and the porous urchin-like Ni-ZnO. (**b**) Bandgap determination from $(\alpha h\upsilon)^2$ vs. $h\upsilon$ of the porous pure sea urchin-like ZnO and the porous sea urchin-like Ni-ZnO.

Figure 5a shows the X-ray photoelectron spectroscopy (XPS) full-scale spectrum of 10% Ni-ZnO sea urchins. All peaks were assigned to the four elements of Zn, Ni, O, and C [13]. The Zn 2p high-resolution XPS is exhibited in Figure 5b. The binding energies at approximately 1044.5 and 1021.7 eV correspond to Zn $2p_{1/2}$ and Zn $2p_{3/2}$, respectively [38]. Figure 5c exhibits the Ni 2p high-resolution XPS. The peaks at ca. 855.2 and 860.8 eV belong to Ni $2p_{3/2}$, and the distinct peaks with binding energies of around 872.6 and 878.5 eV were attributed to the Ni $2p_{1/2}$ [39,40]. This indicates the presence of $Ni^{2+}$ in the Ni-ZnO sea urchins. As displayed in Figure 5d, the O 1s peak was asymmetric, and it can be divided into three peaks. One peak ($O_{lat.}$) at 530.3 eV was assigned to lattice oxygen in wurtzite

ZnO, and the peak ($O_{def.}$) at 530.9 eV corresponds to the defect sites with low-oxygen coordination [41]. The $O_{def.}/O_{lat.}$ value can indicate the oxygen defect concentration in Ni-ZnO sea urchins. Figure S11 presents the O 1s high-resolution XPS spectra of the 5%, 10%, 15%, and 20% Ni-ZnO sea urchins and pure ZnO sea urchins. The $O_{def.}/O_{lat.}$ values of the 5%, 10%, 15%, and 20% Ni-ZnO, and of the pure ZnO sea urchins were 0.34, 0.97, 0.32, 0.47, and 0.31, respectively, as listed in Table S2. The last peak ($O_{ads.}$) at 532.5 eV was due to the physi/chemisorbed $H_2O$. Based on the above analysis results, the 10% Ni-ZnO sea urchins showed the highest oxygen defect concentration among these ZnO-based sea urchin samples, which is due to their high specific surface area and the effect of Ni dopants decreasing the crystal size of ZnO and introducing oxygen-related defects. As for 15% and 20% Ni-ZnO sea urchins, the NiO phase observed in the XRD patterns was verified by the O 1s spectra shown in Figure S11c,d.

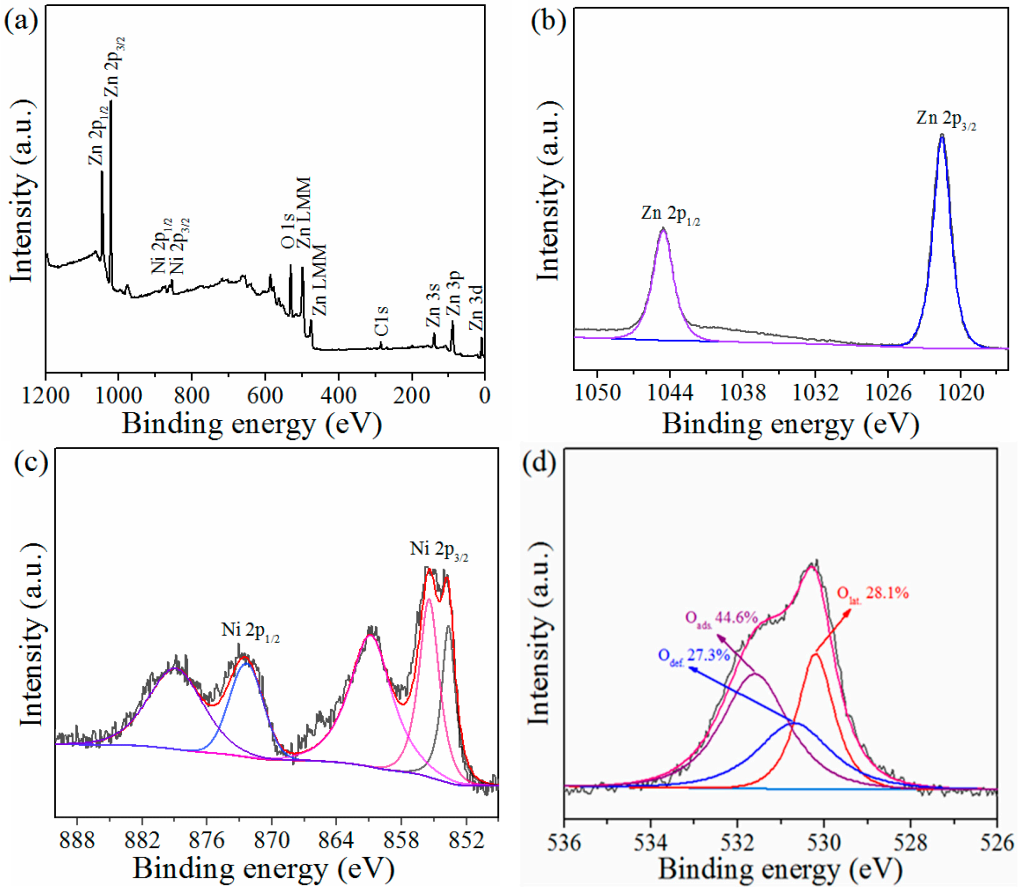


**Figure 5.** XPS spectra of porous urchin-like Ni-ZnO composites: (**a**) survey spectrum, (**b**) Zn 2p, (**c**) Ni 2p, and (**d**) O 1s spectra.

### *3.2. Gas-Sensing Performance*

Figure 6a shows the changes in resistance ($R_a$) of the ZnO and Ni-doped ZnO sea urchin sensors. The working temperatures started from 140 °C to 260 °C. With regard to all the prepared sensors, the $R_a$ value of the sensors decreases as the operating temperature continues to rise. The temperature dependences of the resistance of the obtained samples followed a linear function. The more abundant electrons were forced into a conductance band of the sensing materials activated by the sufficient energy provided by the high temperatures [42]. So, as is well known, the gas sensors belong to the type of surface-controlled one based on the curves changes of resistance temperatures. Under the same working temperature, the $R_a$ sequence of the prepared sensors was present as follows: 20% Ni-ZnO > 15% Ni-ZnO > 10% Ni-ZnO > 5% Ni-ZnO > pure ZnO. This was mainly due to the effect of Ni dopants which can introduce oxygen-related defects [43]. As the

Ni-doped content of the ZnO increases, the crystal size of ZnO decreases and more oxygen molecules are adsorbed on the ultra-small ZnO nanoleaves, forming oxygen ions. In air, these increasing oxygen ions could capture more electrons from ZnO, leading to the higher resistance of the Ni-ZnO sensing film. Furthermore, when the amount of Ni dopants is high, the appearance of NiO and the formation of NiO–ZnO p–n junctions would also increase the resistance of the Ni-ZnO sensing film.

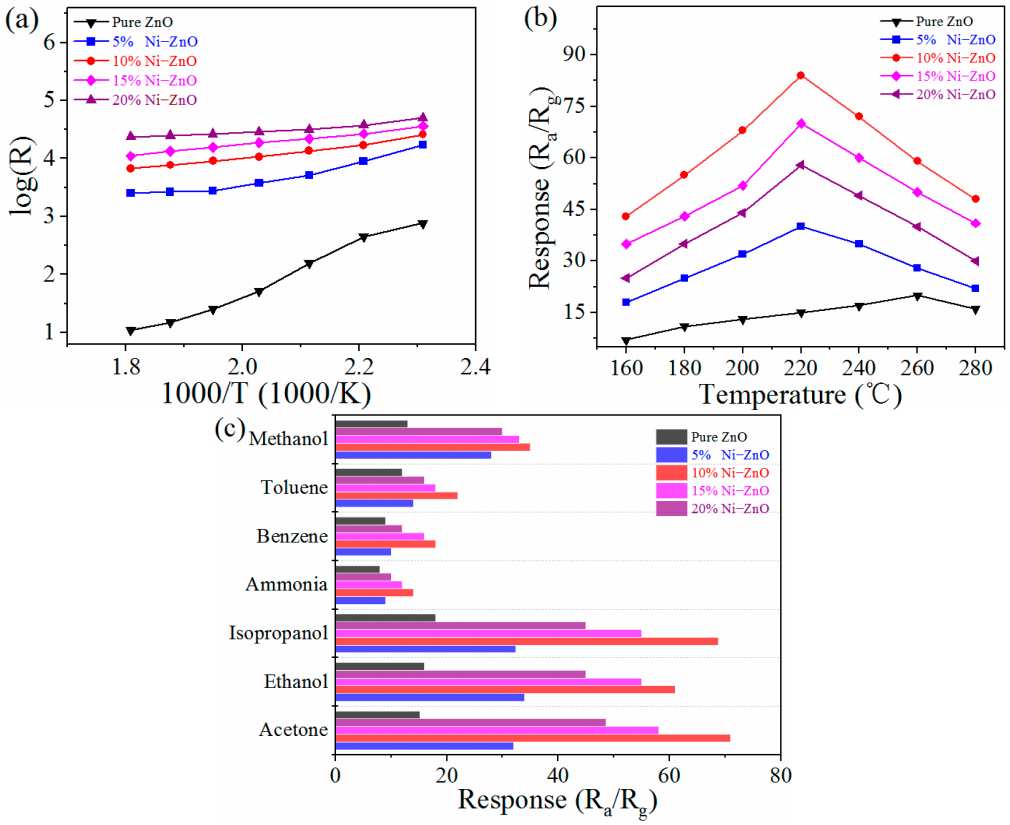


**Figure 6.** (**a**) Resistance of the ZnO-based sensors in air at various working temperatures. (**b**) Responses of ZnO-based sensors upon exposure to 100 ppm formaldehyde vapor at different working temperatures. (**c**) Responses of ZnO-based sensors upon exposure to different gases (100 ppm) at their optimal temperatures.

In Figure 6b, the response of the sensors first increased with increasing working temperature. When the temperature was over 220 °C, however, the response decreased with increasing working temperature. Thus, for the Ni-ZnO sensors, the optimal working temperature can be thought to be 220 °C. This phenomenon conforms to the adsorption/desorption kinetics and thermodynamics on sensing material surface. The gas molecules and oxygen species cannot react fully because of the lack of sufficient energy. When excessive energy was applied to the sensors, the gas molecules adsorbed on the material surface were easily desorbed, resulting in fewer effective surface-absorbed oxygen molecules and targeted molecules. As to the pure ZnO sensor, the optimal working temperature was 260 °C, which is much higher than that of the Ni-ZnO sensors. This demonstrated the decrease in working temperature due to the introduction of Ni dopants. In addition, the response of the Ni-ZnO sea urchin sensor towards 100 ppm formaldehyde vapor was much higher than that of the pure ZnO sea urchin sensor. This was likely attributed to the high concentration of oxygen defects, as verified by XPS. The sample possessed uniform sea urchin-like morphology and larger specific surface area and pore size, likely promoting electron transfer and providing more effective active sites for the redox reaction on the sensing material.

The selectivity of the sensors was studied, as shown in Figure 6c. Among them, the 10% Ni-ZnO sea urchin sensor showed the best sensing performance. The responses for

100 ppm formaldehyde, acetone, ethanol, isopropanol, ammonia, benzene, toluene, and methanol vapors were 84.4, 71.1, 61.8, 68.8, 14.3, 18.2, 22.5, and 35.3, respectively. Therefore, the 10% Ni-ZnO sensor exhibited good sensitivity towards formaldehyde, acetone, ethanol, and isopropanol vapors. Of the sensors, the 10% Ni-ZnO sea urchin sensor exhibited the strongest response to these vapors. Moreover, a good gas-sensing performance was also exhibited by the other sensors for various VOCs. The content of Ni in the ZnO sea urchins has an important effect on the sensors. The presence of oxygen defects enhanced the overall ionic potential of the composites. Thus, the large amount of adsorbed oxygen could strongly capture the material surface. Formaldehyde with a stronger Bronsted acid could react with more adsorbed oxygen ($O_2^-$ and $O^-$) [44].

Figure 7 presents the response curves of different sensors based on pure ZnO, 5%, 10%, 15%, and 20% Ni-ZnO porous sea urchin-like structures exposed to various concentrations of formaldehyde, acetone, ethanol, and isopropanol at an operating temperature of 220 °C. For the 5% Ni-ZnO sensor, the curve of real-time response to formaldehyde gas at different concentrations was observed. The curves in the insets refer to the relationship between the concentration and the response when the sensors are exposed to formaldehyde vapor at different concentrations. In detail, even when exposed to very low concentrations (1 ppm), the response to formaldehyde vapor was close to ca. 6.2. The response was 40.2 when the concentration was increased to 100 ppm. The increasing concentration of detected gases improves the response to formaldehyde, acetone, ethanol, and isopropanol, as shown in the insets. The response to acetone, ethanol, and isopropanol (100 ppm) was 33.6, 34.2, and 32.4, respectively. For the 10% Ni-ZnO sea urchin sensor, the response values to 100 ppm formaldehyde, acetone, ethanol, and isopropanol were 84.4, 71.1, 61.8, and 68.8, respectively. In addition, the 15% Ni-ZnO sea urchin sensor, the 20% Ni-ZnO sea urchin sensor, and the pure ZnO sea urchin sensor showed response values to formaldehyde of 70.4, 62.2, and 20.5, respectively, to acetone of 58.1, 48.6, and 15.2, respectively, to ethanol of 55.2, 45.1, and 16.9, respectively, and to isopropanol of 55.9, 45.7, and 18.5, respectively. Furthermore, for 100 ppm formaldehyde vapor, the response and recovery times were also investigated, as exhibited in Figure S12. The response times (~22 s, ~17 s, ~19 s, ~20 s, and ~22 s) and the recovery times (~30 s, ~20 s, ~22 s, ~24 s, and ~32 s) were obtained for 5%, 10%, 15%, 20% Ni-ZnO, and pure ZnO sea urchin sensors, respectively. Compared to the other sensors, the 10% Ni-ZnO sensor with the largest specific surface area exhibited superior gas-sensing behaviors upon exposure to formaldehyde, acetone, ethanol, and isopropanol vapors. The largest specific surface area could hold more passages and "surface accessibility" to accelerate the transfer of the target molecule. This leads to an easy gas molecule (detected gases or oxygen) adsorption/dissociation from the sensing materials attributed to the production of more active sites. Moreover, the excellent sensing performance was attributed to the smaller size of porous nanoleaves and the smaller size of the pores distributed over the surface of the numerous nanoleaves. In general, the specific surface area, Ni-doping content, and porous sea urchin-like structure jointly affect the sensing properties. Compared to ZnO-based sensors, the 10% Ni-ZnO sensors presented better sensing behaviors to formaldehyde vapor than 3 mol% NiO/ZnO microflowers [45], CdO-ZnO nanorices [46], 3 wt.% Ag-$In_2O_3$/ZnO nanocomposites [47], $SnO_2$-ZnO/PdO nanoparticles [48], ZnO/$SnO_2$ hollow nanospheres [49], $Co_3O_4$/ZnO hollow spheres [50], and 1% Er-ZnO nanowires [51], as listed in Table S3.

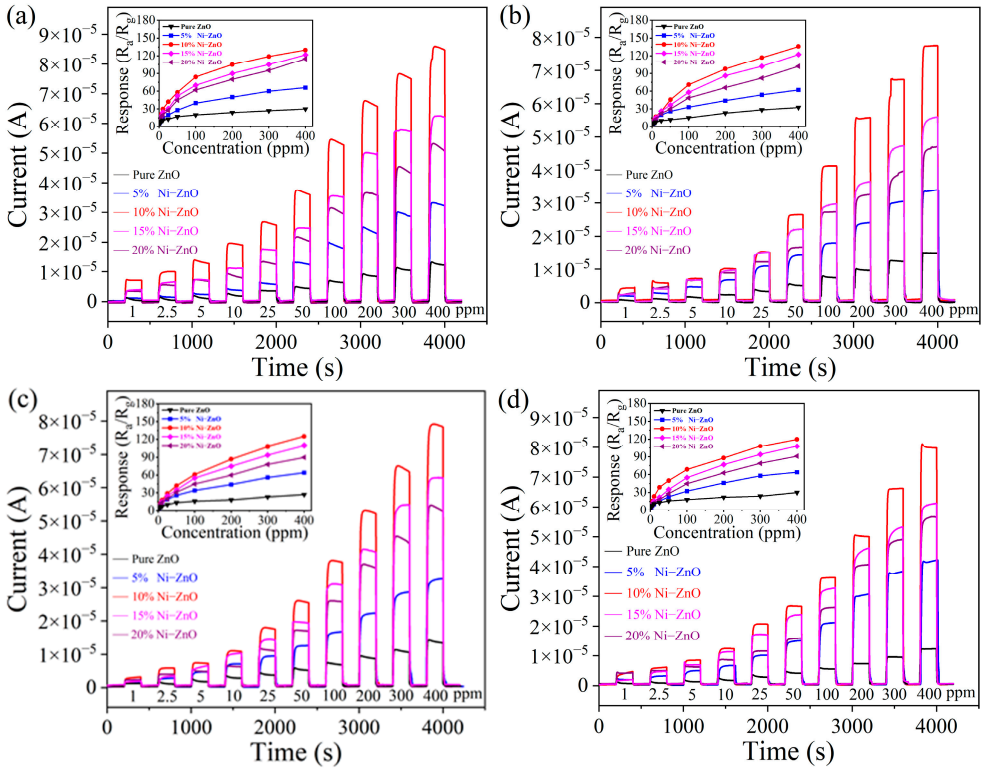


**Figure 7.** Real-time response curves of the sensor devices upon exposure to different concentrations of (**a**) formaldehyde, (**b**) acetone, (**c**) ethanol, and (**d**) isopropanol at a working temperature of 220 °C. The insets show the corresponding sensor response curves.

Figure 8a shows ten reversible cycles of the sea urchin-shaped Ni-ZnO sensor upon exposure to 100 ppm formaldehyde vapor. When the sensor comes in contact with formaldehyde vapor, the current quickly rises to a high level. The current decreases sharply to the initial level when the sensor is off formaldehyde vapor. The response currents of the sensors were stable and repeatable. Therefore, all Ni-ZnO sea urchin sensors showed excellent cycling stability and repeatability for detecting VOCs. Furthermore, Figure 8b shows the good linear relationship of the responses of the prepared sensors to the various concentrations of formaldehyde. Linear regression coefficients ($R^2$) of the 5%, 10%, 15%, and 20% Ni-ZnO sea urchin sensors, and of the pure ZnO sea urchin sensor, were 0.978, 0.991, 0.977, 0.978, and 0.931, respectively. Clearly, the 10% Ni-ZnO sea urchin sensor shows a better linear relationship between the response and formaldehyde concentration.

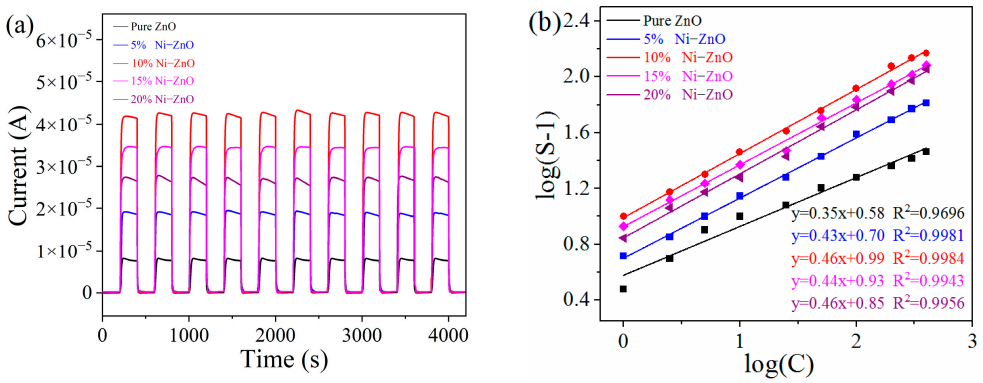


**Figure 8.** (**a**) Current change curves of the 10% Ni-ZnO sensor upon exposure to 100 ppm formaldehyde vapor for 10 tests at the optimal working temperature (220 °C). (**b**) Linear relationship of the response to different concentrations of formaldehyde.

### *3.3. Gas-Sensing Mechanism*

The sensing mechanism of the ZnO-based sensor was attributed to the surface adsorbed oxygen species and the redox reactions between the target gases and the oxygen species, which leads to variations in the sensor resistance. For the pure ZnO sensor, when the sensor is exposed to the air, oxygen molecules will adsorb on ZnO surface, generating thin electron depletion layers. Electrons in the ZnO conduction band are drawn by oxygen molecules to form oxygen species with strong oxidizing properties ($O_2^-$ and $O^-$). Each target gas is dissociated/ionized on the ZnO surface and reacts with ionosorbed oxygen elements ($O_2^-$, $O^-$, and $O_2$), forming $H_2O$ (g) and $CO_2$ (g). The enhancement of the conductivity will be produced due to a thinner electron depletion layer as the number of adsorbed oxygen decreases. Consequently, the electrons return into the ZnO conduction band when surface catalytic reactions occur between oxygen anions and HCHO (see Equation (3)). Compared to pure ZnO sea urchins, the sensing performance of Ni-ZnO sea urchin sensors was improved greatly, which can be attributed to the increase of the charge transfer by doping, producing electronic sensitization that makes ZnO more sensitive to VOC vapors. The Ni-doped ZnO nanocrystals provide abundant active sites for formaldehyde molecule adsorption which, combined with defects of Ni-doped ZnO nanocrystals, can generate the intermediates and react with absorbed oxygen on Ni-doped ZnO (see Equations (4) and (5)). Therefore, Ni dopants can lead to the dissociation and ionization of VOCs, making ZnO more sensitive and selective. The addition of Ni increased the VOC adsorption amount on the surface and accelerated its ionization [51,52]. This process decreases the working temperature of the sensor due to water formation.

$$HCHO_{(ads)} + 2O^-(O_2^-) \rightarrow CO_2 + H_2O + 2e^- \quad (3)$$

$$HCHO_{(ads)} + h^+ + O^-(O_2^-) \rightarrow HCOOH \quad (4)$$

$$HCHO_{(ads)} + 2h^+ + 2O^-(O_2^-) \rightarrow CO_2 + H_2O \quad (5)$$

Moreover, the sensing property of the ZnO-based sensor depends greatly on its average grain diameter (D) [52]. When $D \leq 2L$ (L = thickness of the depletion layer), the grain can be fully depleted, and its conductance is grain-controlled [18]. The diameter of the ZnO crystallites (10% Ni-ZnO) averaged around 12.5 nm, which is the same as the ZnO Debye length ($L_D$) [18], indicating that 10% Ni-ZnO are almost fully depleted. The nanosize effect implies that many surface zinc atoms can play an important part in surface catalytic reactions. Furthermore, the largest specific surface area (116.5 $m^2\ g^{-1}$) could hold more passages and "surface accessibility" to accelerate the transfer of the target molecule. This leads to an easy gas molecule (detected gases or oxygen) adsorption/dissociation from the sensing materials, attributed to the production of more active sites. On the other hand, due to the difference of lattice spacing, some defects and vacancies could be created near the region of n-ZnO/p-NiO heterocontacts, which will lead to more active sites for gas adsorption and surface reaction compared with pure ZnO. Therefore, the Ni-ZnO sea urchins as sensing materials can improve sensitivity and shorten response/recovery times significantly.

## 4. Conclusions

The Ni-ZnO sea urchins consisting of numerous porous nanoleaves were prepared by an aqueous solution method and a subsequent heat treatment. The Ni-ZnO sea urchins with various amounts of Ni dopants possessed small nanocrystals and a high specific surface area. Used as sensing material, they exhibited a strong response, fine stability, and short response–recovery times for detecting formaldehyde vapor. Furthermore, among these ZnO-based gas sensors, the 10% Ni-ZnO sea urchin sensor exhibited the highest gas-sensing performance towards some VOC vapors, such as formaldehyde, acetone,

ethanol, and isopropanol. The high specific surface area, stable 3D porous structure, and moderate content of Ni dopants with a high content of oxygen defects contribute to the surface catalytic reaction, gas absorption–desorption, and effective electron transfer in the gas-sensing process.

**Supplementary Materials:** The following supporting information can be downloaded at: https://www.mdpi.com/article/10.3390/chemosensors11040223/s1. Figure S1: Experimental setup; Figure S2: (a) Photograph of the sensor and (b) diagram of the testing principle of the gas-sensing measurement system ($V_h$: heating voltage); Figure S3: XRD patterns of (a) $Zn_5(CO_3)_2(OH)_6$ precursor and calcined ZnO product, and (b) EDS analysis of 10% Ni-ZnO product; Figure S4: SEM images of (a) 5% Ni-$Zn_5(CO_3)_2(OH)_6$ precursor and (b) calcined 5% Ni-ZnO product. SEM images of (c) 15% Ni-$Zn_5(CO_3)_2(OH)_6$ precursor and (d) calcined 15% Ni-ZnO product. SEM images of (e) 20% Ni-$Zn_5(CO_3)_2(OH)_6$ precursor and (f) calcined 20% Ni-ZnO product; Figure S5: (a) SEM image and corresponding EDS mapping images of the sea urchin-like 10% Ni-ZnO product: (b) Ni, (c) Zn, and (d) O; Figure S6: SEM images of (a,b) the $Zn_5(CO_3)_2(OH)_6$ precursor and (c,d) the calcined ZnO product; Figure S7: TGA curves of the sea urchin-like Ni-doped $Zn_5(CO_3)_2(OH)_6$ precursor; Figure S8: FTIR spectra of (a) the sea urchin-like 10% Ni-$Zn_5(CO_3)_2(OH)_6$ precursor and (b) sea urchin-like 10% Ni-ZnO; Figure S9: Nitrogen adsorption and desorption isotherms of (a) 5% Ni-ZnO, (b) 10% Ni-ZnO, (c) 15% Ni-ZnO, and (d) 20% Ni-ZnO sea urchins. The insets show the corresponding pore size distributions TGA curves of sea urchin-like Ni-doped $Zn_5(CO_3)_2(OH)_6$ precursor; Figure S10: Nitrogen adsorption–desorption isotherms of pure urchin-like ZnO. The inset is the corresponding pore size distribution; Figure S11: O 1s high-resolution XPS spectrum of (a) 5%, (b) 10%, (c) 15%, and (d) 20% Ni-ZnO sea urchins, and (e) pure ZnO sea urchins; Figure S12: Dynamic response-recovery curves of porous urchin-like Ni-ZnO sensors and the porous urchin-like ZnO sensor towards 100 ppm formaldehyde; Table S1: Structural parameters of Ni-doped ZnO sea urchins according to the Joint Committee on Powder Diffraction Standards (JCPDS no. 36-1451 (a = 3.250 Å and c = 5.207 Å)); Table S2: Fitting results of the O 1s XPS spectra of Ni-ZnO and pure ZnO sea urchins; Table S3: Responses of various ZnO-based sensing materials to different concentrations of formaldehyde vapor.

**Author Contributions:** Conceptualization, H.W.; methodology, H.W., X.D. and H.R.; validation, H.R.; investigation, H.W. and X.D.; resources, J.H. and S.W.J.; writing—original draft preparation, H.W.; writing—review and editing, J.H. and S.W.J.; supervision, H.R.; funding acquisition, S.W.J. All authors have read and agreed to the published version of the manuscript.

**Funding:** This research was funded by the National Research Foundation of Korea (NRF-2019R1A 5A8080290), Breeding Project of Anhui Polytechnic University (KZ42022076) and Open Research Found of Anhui Key Laboratory of High-performance Non-ferrous Metal Materials (YSJS-2023-07).

**Institutional Review Board Statement:** Not applicable.

**Informed Consent Statement:** Not applicable.

**Data Availability Statement:** The data presented in this study are available on request from the corresponding author.

**Conflicts of Interest:** The authors declare no conflict of interest.

## References

1. Shooshtari, M.; Salehi, A. An electronic nose based on carbon nanotube-titanium dioxide hybrid nanostructures for detection and discrimination of volatile organic compounds. *Sens. Actuators B Chem.* **2018**, *357*, 131418. [CrossRef]
2. Broza, Y.; Vishinkin, R.; Barash, O.; Nakhleh, M.; Haick, H. Synergy between nanomaterials and volatile organic compounds for non-invasive medical evaluation. *Chem. Soc. Rev.* **2018**, *47*, 4781–4859. [CrossRef]
3. Kim, K.; Choi, P.; Itoh, T.; Masuda, Y. Catalyst-free highly sensitive $SnO_2$ nanosheet gas sensors for parts per billion-level detection of acetone. *ACS Appl. Mater. Interfaces* **2020**, *12*, 51637–51644. [CrossRef]
4. Huang, B.; Zeng, W.; Li, Y. Synthesis of ZIF-8 coating on ZnO nanorods for enhanced gas-sensing performance. *Chemosensors* **2022**, *10*, 297. [CrossRef]
5. Zhang, S.; Lin, Z.; Song, P.; Sun, J.; Wang, Q. MOF-derived $In_2O_3$ nanotubes/$Cr_2O_3$ nanoparticles composites for superior ethanol gas-sensing performance at room temperature. *Ceram. Int.* **2022**, *48*, 28334–28342. [CrossRef]

6. Wang, M.; Wang, Y.; Li, X.; Ge, C.; Hussain, S.; Liu, G.; Qiao, G. $WO_3$ porous nanosheet arrays with enhanced low temperature $NO_2$ gas sensing performance. *Sens. Actuators B Chem.* **2020**, *316*, 128050. [CrossRef]
7. Li, Q.; Zeng, W.; Zhou, Q.; Wang, Z. Highly sensitive ethanol sensing using NiO hollow spheres synthesized via hydrothermal method. *Chemosensors* **2022**, *10*, 341. [CrossRef]
8. Vijayakumar, Y.; Nagaraju, P.; Sreekanth, T.; Rushidhar, U.; Reddy, P. Effect of precursor volume on chemically sprayed $V_2O_5$ thin films for acetaldehyde detection. *Superlattices Microstruct.* **2021**, *153*, 106870. [CrossRef]
9. Beitollahi, H.; Tajik, S.; Nejad, F.; Safaei, M. Recent advances in ZnO nanostructure-based electrochemical sensors and biosensors. *J. Mater. Chem. B* **2020**, *8*, 5826–5844. [CrossRef]
10. Liu, B.H.; Wang, S.; Yuan, Z.; Duan, Z.H.; Zhao, Q.N.; Zhang, Y.J.; Su, Y.J.; Jiang, Y.D.; Xie, G.Z.; Tai, H.L. Novel chitosan/ZnO bilayer film with enhanced humidity-tolerant property: Endowing triboelectric nanogenerator with acetone analysis capability. *Nano Energy* **2020**, *78*, 105256. [CrossRef]
11. Cui, X.S.; Lu, Z.R.; Wang, Z.C.; Zeng, W.; Zhou, Q. Highly sensitive $SF_6$ decomposition byproducts sensing platform based on CuO/ZnO heterojunction nanofibers. *Chemosensors* **2023**, *11*, 58. [CrossRef]
12. Dilova, T.; Atanasova, G.; Dikovska, A.; Nedyalkov, N. The effect of light irradiation on the gas-sensing properties of nanocomposites based on ZnO and Ag nanoparticles. *Appl. Surf. Sci.* **2020**, *505*, 144625. [CrossRef]
13. Si, W.; Du, W.; Wang, F.; Wu, L.; Liu, J.; Liu, W.; Cui, P.; Zhang, X. One-pot hydrothermal synthesis of nano-sheet assembled NiO/ZnO microspheres for efficient sulfur dioxide detection. *Ceram. Int.* **2020**, *46*, 7279–7287. [CrossRef]
14. Dang, T.; Son, N.; Lanh, N.; Phuoc, P.; Viet, N.; Thong, L.; Hung, C.; Duy, N.; Hoa, N.; Hieu, N. Extraordinary $H_2S$ gas sensing performance of ZnO/rGO external and internal heterojunctions. *J. Alloy. Compd.* **2021**, *879*, 160457. [CrossRef]
15. Yuan, Z.; Feng, Z.; Kong, L.; Zhan, J.; Ma, X. Simple synthesis of porous ZnO nanoplates hyper-doped with low concentration of Pt for efficient acetone sensing. *J. Alloy. Compd.* **2021**, *865*, 158890. [CrossRef]
16. Cao, P.; Yang, Z.; Navale, S.; Han, S.; Liu, X.; Liu, W.; Lu, Y.; Stadler, F.; Zhu, D. Ethanol sensing behavior of Pd-nanoparticles decorated ZnO-nanorod based chemiresistive gas sensors. *Sens. Actuators B Chem.* **2019**, *298*, 126850. [CrossRef]
17. Ahemad, M.; Le, T.; Kim, D.; Yu, Y. Bimetallic AgAualloy@ZnO core-shell nanoparticles for ultra-high detection of ethanol: Potential impact of alloy composition on sensing performance. *Sens. Actuators B Chem.* **2022**, *359*, 131595. [CrossRef]
18. Drmosh, Q.; Wajih, Y.; Alade, I.; Mohamedkhair, A.; Qamar, M.; Hakeem, A.; Yamani, Z. Engineering the depletion layer of Au-modified ZnO/Ag core-shell films for high-performance acetone gas sensing. *Sens. Actuators B Chem.* **2021**, *338*, 129851. [CrossRef]
19. Guo, W.; Zhao, B.; Zhou, Q.; He, Y.; Wang, Z.; Radacsi, N. Fe-doped ZnO/reduced graphene oxide nanocomposite with synergic enhanced gas sensing performance for the effective detection of formaldehyde. *ACS Omega* **2019**, *4*, 10252–10262. [CrossRef]
20. Mo, Y.; Shi, F.; Qin, S.; Tang, P.; Feng, Y.; Zhao, Y.; Li, D. Facile fabrication of mesoporous hierarchical Co-doped ZnO for highly sensitive ethanol detection. *Ind. Eng. Chem. Res.* **2019**, *58*, 8061–8071. [CrossRef]
21. Elkhalidi, Z.; Hartiti, B.; Siadat, M.; Comini, E.; Arachchige, H.; Fadili, S.; Thevenin, P. Acetone sensor based on Ni doped ZnO nanostructues: Growth and sensing capability. *J. Mater. Sci. Mater. Electron.* **2019**, *30*, 7681–7690. [CrossRef]
22. Rahman, M. Efficient formaldehyde sensor development based on Cu-codoped ZnO nanomaterial by an electrochemical approach. *Sens. Actuators B Chem.* **2020**, *305*, 127541. [CrossRef]
23. Namgung, G.; Ta, Q.; Yang, W.; Noh, J. Diffusion-driven Al-doping of ZnO nanorods and stretchable gas sensors made of doped ZnO nanorods/Ag nanowires bilayers. *ACS Appl. Mater. Interfaces* **2019**, *11*, 1411–1419. [CrossRef]
24. Kamble, V.; Navale, Y.; Patil, V.; Desai, N.; Salunkhe, S. Enhanced $NO_2$ gas sensing performance of Ni-doped ZnO nanostructures. *J. Mater. Sci. Mater. Electron.* **2021**, *32*, 2219–2233. [CrossRef]
25. Badawi, A.; Althobaiti, M.; Ali, E.; Alharthi, S.; Alharbi, A. A comparative study of the structural and optical properties of transition metals (M = Fe, Co, Mn, Ni) doped ZnO films deposited by spray-pyrolysis technique for optoelectronic applications. *Opt. Mater.* **2022**, *124*, 112055. [CrossRef]
26. Jiang, B.; Yang, S. Nickel-doped ZnO nanowalls with enhanced electron transport ability for electrochemical water splitting. *Nanomaterials* **2021**, *11*, 1980. [CrossRef]
27. Minhas, H.; Kumar, D.; Kumar, A. Preparation, characterization and electromagnetic interference shielding effect of Ni-doped ZnO thin films. *Mater. Res. Express* **2019**, *6*, 105049. [CrossRef]
28. Modaberi, M.; Rooydell, R.; Brahma, S.; Akande, A.; Mwakikunga, B.; Liu, C. Enhanced response and selectivity of $H_2S$ sensing through controlled Ni doping into ZnO nanorods by using single metal organic precursors. *Sens. Actuators B Chem.* **2018**, *273*, 1278–1290. [CrossRef]
29. Bhati, V.; Ranwa, S.; Fanetti, M.; Valant, M.; Kumar, M. Efficient hydrogen sensor based on Ni-doped ZnO nanostructures by RF sputtering. *Sens. Actuators B Chem.* **2018**, *255*, 588–597. [CrossRef]
30. Wu, J.; Li, T.; Meng, G.; Xiang, Y.; Hai, J.; Wang, B. Carbon nanofiber supported Ni-ZnO catalyst for efficient and selective hydrogenation of pyrolysis gasoline. *Catal. Sci. Technol.* **2021**, *11*, 4216–4225. [CrossRef]
31. Zhang, S.; Li, Y.; Sun, G.; Zhang, B.; Wang, Y.; Cao, J.; Zhang, Z. Synthesis of NiO-decorated ZnO porous nanosheets with improved $CH_4$ sensing performance. *Appl. Surf. Sci.* **2019**, *497*, 143811. [CrossRef]
32. Zhang, H.; Chen, W.; Li, Y.; Song, Z.; Zeng, W.; Tang, S.; Wang, S.; Zhou, D. Hierarchical heterostructures of nanosheet-assembled NiO-modified ZnO microflowers for high performance acetylene detection. *Ceram. Int.* **2020**, *46*, 3574–3581. [CrossRef]

33. Lei, C.S.; Pi, M.; Cheng, B.; Jiang, C.J.; Qin, J.Q. Fabrication of hierarchical porous ZnO/NiO hollow microspheres for adsorptive removal of Congo red. *Appl. Surf. Sci.* **2018**, *435*, 1002–1010. [CrossRef]
34. Cun, T.; Dong, C.; Huang, Q. Ionothermal precipitation of highly dispersive ZnO nanoparticles with improved photocatalytic performance. *Appl. Surf. Sci.* **2016**, *384*, 73–82. [CrossRef]
35. Niu, H.; Zhou, D.; Yang, X.; Li, X.; Wang, Q.; Qu, F. Towards three-dimensional hierarchical ZnO nanofiber@Ni(OH)$_2$ nanoflake core-shell heterostructures for high-performance asymmetric supercapacitors. *J. Mater. Chem. A* **2015**, *3*, 18413–18421. [CrossRef]
36. Starukh, G.; Rozovik, O.; Oranska, O. Organo/Zn-Al LDH nanocomposites for cationic dye removal from aqueous media. *Nanoscale Res. Lett.* **2016**, *11*, 228–237. [CrossRef]
37. Mao, Y.; Cheng, Y.; Wang, J.; Yang, H.; Li, M.; Chen, J.; Chao, M.; Tong, Y.; Liang, E. Amorphous NiO electrocatalyst overcoated ZnO nanorod photoanodes for enhanced photoelectrochemical performance. *New J. Chem.* **2016**, *4*, 107. [CrossRef]
38. Su, C.; Zhang, L.; Han, Y.; Ren, C.; Li, B.; Wang, T.; Zeng, M.; Su, Y.; Hu, N.; Zhou, Z.; et al. Glucose-assisted synthesis of hierarchical NiO-ZnO heterostructure with enhanced glycol gas sensing performance. *Sens. Actuators B Chem.* **2021**, *329*, 129167. [CrossRef]
39. Ouyang, Y.; Xia, X.; Ye, H.; Wang, L.; Jiao, X.; Lei, W.; Hao, Q. Three-dimensional hierarchical structure ZnO@C@NiO on carbon cloth for asymmetric supercapacitor with enhanced cycle stability. *ACS Appl. Mater. Inter.* **2018**, *10*, 3549–3561. [CrossRef] [PubMed]
40. Bhatia, P.; Nath, M. Green synthesis of p-NiO/n-ZnO nanocomposites: Excellent adsorbent for removal of congo red and efficient catalyst for reduction of 4-nitrophenol present in wastewater. *J. Water Process Eng.* **2020**, *33*, 101017. [CrossRef]
41. Zhou, Q.; Zeng, W.; Chen, W.; Xu, L.; Kumar, R.; Umar, A. High sensitive and low-concentration sulfur dioxide ($SO_2$) gas sensor application of heterostructure NiO-ZnO nanodisks. *Sens. Actuators B Chem.* **2019**, *298*, 126870. [CrossRef]
42. Wei, S.; Wang, S.; Zhang, Y.; Zhou, M. Different morphologies of ZnO and their ethanol sensing property. *Sens. Actuators B Chem.* **2014**, *192*, 480–487. [CrossRef]
43. Yuan, Z.; Li, J.; Meng, F. High response n-propanol sensor based on co-modified ZnO nanorods. *J. Alloy. Compd.* **2022**, *910*, 164971. [CrossRef]
44. Gao, L.; Fu, H.; Zhu, J.; Wang, J.; Chen, Y.; Liu, H. Synthesis of $SnO_2$ nanoparticles for formaldehyde detection with high sensitivity and good selectivity. *J. Mater. Res.* **2020**, *35*, 2208–2217. [CrossRef]
45. San, X.; Li, M.; Liu, D.; Wang, G.; Shen, Y.; Meng, D.; Meng, F. A facile one-step hydrothermal synthesis of NiO/ZnO heterojunction microflowers for the enhanced formaldehyde sensing properties. *J. Alloy. Compd.* **2018**, *739*, 260–269. [CrossRef]
46. Umar, A.; Ibrahim, A.; Kumar, R.; Algadi, H.; Albargi, H.; Alsairi, M.; Alhmami, M.; Zeng, W.; Ahmed, F.; Akbar, S. CdO-ZnO nanorices for enhanced and selective formaldehyde gas sensing applications. *Environ. Res.* **2021**, *200*, 111377. [CrossRef]
47. Dong, C.; Xu, L.; Hang, B.; Deng, S.; Xiao, X.; Wang, Y. Nonaqueous synthesis of Ag-functionalized $In_2O_3$/ZnO nanocomposites for highly sensitive formaldehyde sensor. *Sens. Actuators B Chem.* **2016**, *224*, 193–200. [CrossRef]
48. Jiao, S.; Xue, W.; Zhang, C.; Li, F.; Meng, B.; Zhan, Z. Improving the formaldehyde gas sensing performance of the ZnO/$SnO_2$ nanoparticles by PdO decoration. *J. Mater. Sci. Mater. Electron.* **2020**, *31*, 684–692.
49. Sun, Y.; Yang, H.; Zhao, Z.; Suematsu, K.; Li, P.; Yu, Z.; Zhang, W.; Hu, J. Fabrication of ZnO quantum dots@$SnO_2$ hollow nanospheres hybrid hierarchical structures for effectively detecting formaldehyde. *Sens. Actuators B Chem.* **2020**, *318*, 128222. [CrossRef]
50. Bai, S.; Guo, J.; Shu, X.; Xiang, X.; Luo, R.; Li, D.; Chen, A.; Liu, C. Surface functionalization of $Co_3O_4$ hollow spheres with ZnO nanoparticles for modulating sensing properties of formaldehyde. *Sens. Actuators B Chem.* **2017**, *245*, 359–368. [CrossRef]
51. Zhao, S.; Shen, Y.; Li, A.; Chen, Y.; Gao, S.; Liu, W.; Wei, D. Effects of rare earth elements doping on gas sensing properties of ZnO nanowires. *Ceram. Int.* **2021**, *47*, 24218–24226. [CrossRef]
52. Han, M.; Kim, H.; Lee, H.; Park, J.; Lee, H. Effects of porosity and particle size on the gas sensing properties of $SnO_2$ films. *Appl. Surf. Sci.* **2019**, *481*, 133–137. [CrossRef]